

Adaptive Uncertainty-Guided Model Selection for Data-Driven PDE Discovery

Pongpisit Thanasutives¹, Takashi Morita², Masayuki Numao², Ken-ichi Fukui²

¹Graduate School of Information Science and Technology, Osaka University, Osaka, Japan

²SANKEN (The Institute of Scientific and Industrial Research), Osaka University, Osaka, Japan
{thanasutives, t-morita, numao, fukui}@ai.sanken.osaka-u.ac.jp

Abstract

We propose a new parameter-adaptive uncertainty-penalized Bayesian information criterion (UBIC) to prioritize the parsimonious partial differential equation (PDE) that sufficiently governs noisy spatial-temporal observed data with few reliable terms. Since the naive use of the BIC for model selection has been known to yield an undesirable overfitted PDE, the UBIC penalizes the found PDE not only by its complexity but also the quantified uncertainty, derived from the model supports' coefficient of variation in a probabilistic view. We also introduce physics-informed neural network learning as a simulation-based approach to further validate the selected PDE flexibly against the other discovered PDE. Numerical results affirm the successful application of the UBIC in identifying the true governing PDE. Additionally, we reveal an interesting effect of denoising the observed data on improving the trade-off between the BIC score and model complexity. Code is available at <https://github.com/Pongpisit-Thanasutives/UBIC>.

Introduction

Data-driven discovery has emerged as a popular approach for uncovering the governing partial differential equation (PDE) of a dynamical system, offering flexibility and satisfactory accuracy without relying heavily on domain knowledge. Sparse regression is typically leveraged to approximate a linear combination of user-specified candidate terms that optimally balances between a capability to predict temporal dynamics and the model complexity, hence so-called SINDy (sparse identification of nonlinear dynamics)-based approaches (Brunton, Proctor, and Kutz 2016), which were successfully applied in diverse disciplines from aerodynamics (Li et al. 2019), biological transport (Lagergren et al. 2020) to epidemiology (Horrocks and Bauch 2020).

Diverse regularized regressors, designed to achieve the sparse identification were, for example, STRidge (sequential threshold ridge regression in PDE-FIND) (Rudy et al. 2017), LASSO (least absolute shrinkage and selection operator) (Tibshirani 1996) and SR3 (Sparse relaxed regularized regression) (Zheng et al. 2018). However, tuning the regularization hyperparameter(s) of these methods for model selection is challenging, because the chosen hyperparameter may deliver an overfitted model. Also, it is difficult to control the model complexity. As a result, there is a risk of overlooking the true governing equation of a particular complexity.

The mixed-integer optimization (MIO) for best-subset selection (Bertsimas, King, and Mazumder 2016) has been introduced to customize the desirable sparsity in the provably optimal MIO-SINDy (Bertsimas and Gurnee 2023). Various best-subset solvers are utilized to collect potential PDEs, from which one is automatically selected as the most suitable underlying PDE by an algorithm (Thanasutives et al. 2023). Although impressive progress has been made in deliberate consideration of likely PDEs consecutively arranged with a maximum complexity constraint, the important question remains: *How do we select the best model that reveals the true governing PDE form?*

Before the model selection, we assure the existence of such a suitable PDE within our collection of potential models by enhancing the quality of the observed data, which are maybe noisy. A few previous attempts to denoise the distorted observed data (and its derivatives) were through derivative computation using polynomials, spline-based models, and Robust PCA (principal component analysis) (Rudy et al. 2017; Sun et al. 2022; Li et al. 2020). To simplify the experimental design, we concentrate on our preferred choices of denoising techniques that have numerically shown a positive impact on the model selection step: the regularized KSVD (Dumitrescu and Irofti 2017), a dictionary learning generalizing the K-means clustering.

In the model selection given a finite set of potential PDEs, Akaike information criterion (AIC) (Akaike 1974; Mangan et al. 2017; Dong et al. 2023) and Bayesian information criterion (BIC) (Schwarz 1978) are commonly adopted as metrics evaluating point estimates of model parameters. However, in practice, the AIC and BIC values associated with a sequence of complexity-increasing linear models, fitted on an overcomplete candidate library to estimate temporal dynamics, tend to decrease, albeit insignificantly, after even the actual PDE is found. Therefore, naively selecting the PDE that minimizes the information criterion, could lead to erroneous equations (Thanasutives et al. 2023).

In this paper, we suggest a new way to assess the goodness of an approximated model by quantifying its associated uncertainty. We go beyond point estimates of the model parameters or coefficients and instead put a posterior belief on them. For each potential PDE, Bayesian linear regression is modeled on its corresponding subset to obtain the posterior distribution of the coefficients. Then, the coefficients'

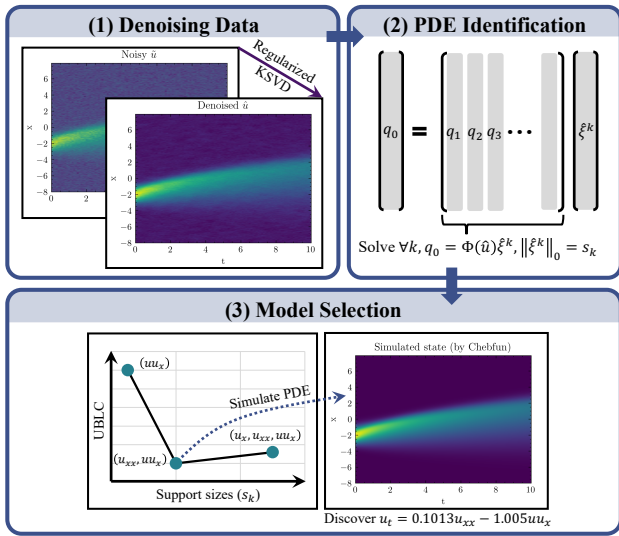


Figure 1: Schematic diagram of the Burgers' PDE discovery example incorporating the UBIC for the model selection

mean and covariance are computed, generally through certain posterior samples or analytical methods (if available), to quantify the uncertainty based on the coefficient of variation. By this means, we gain insights into the reliability of the estimated coefficients, which is, in turn, exploited adaptively by our proposed uncertainty-penalized Bayesian information criterion (UBIC). Figure 1 visualizes the primary steps to discover the underlying PDE starting from the denoising data to model selection.

The UBIC-selected PDE can be optionally validated using simulation-based model selection, measuring the BIC of the PDE simulated state solution for directly predicting the denoised observed data. We investigate the use of a physics-informed neural network (PINN) (Raissi, Perdikaris, and Karniadakis 2019) as a differentiable automatic PDE solver. By incorporating physical laws as a part of its learning constraints, PINN enables the flexible PDE-solving approach.

We list the main contributions in what follows.

- The UBIC integrates the quantified uncertainty of each potential PDE to penalize the BIC, resulting in the true identification of the parsimonious and stable governing PDE without heavy reliance on hyperparameter tuning.
- We numerically exhibit the positive impact of denoising in terms of improving the trade-off given by the BIC.
- We explore the simulation-based model selection that evaluates the efficiency of the PDE state solution, simulated by a PINN, in predicting the denoised data directly.

Bayesian PDE Discovery Methods Although such uncertainty-quantified SINDy (UQ-SINDy) (Hirsh, Barajas-Solano, and Kutz 2022) and threshold sparse Bayesian regression with error bars (Zhang and Lin 2018), were previously introduced, the uncertainty-guided model selection remains underexplored. Notably, the UQ-SINDy employed sparsifying priors to induce nonzeros terms identified with

their posterior inclusion probabilities generally once, leading to risks of missing some correct terms or including incorrect ones. The latter work also risked excluding small yet important PDE coefficients due to a sensitive threshold. The comparisons are discussed thoroughly in the supplement.

Methodology

Problem Formulation

Let us assume without loss of generality that the system state u in a two-dimensional (2D) spatio-temporal grid of spatially distributed physical systems satisfies

$$\partial_t u = \mathcal{N}(u, \partial_x u, \partial_x^2 u, \dots; \xi). \quad (1)$$

We aim to discover \mathcal{N} , a linear or nonlinear operator involving spatial derivatives of the state variable u only. Parametric dependency ξ_j is a constant vector-valued coefficient. For convenience, we consider $\partial_x u \equiv u_x$ and other notations alike. Since our observation input \tilde{u} may be disturbed with noise, or mathematically $\tilde{u}_{ij} = u(x_i, t_j) + z(x_i, t_j)$, we begin our PDE discovery approach by denoising on \tilde{u} .

Noise $z(x_i, t_j) \sim \frac{\epsilon \sigma_u}{100} \mathcal{N}(0, 1)$ is drawn from standard Gaussian distribution, and scaled proportionally to $\epsilon\%$ of the standard deviation (sd) σ_u calculated over the domain.

Denoising Data

Suppose the grid is in a two-dimensional (2D) space, we turn \tilde{u} into a zero-mean array stacking flattened patches, regarded as signals $S_p(\tilde{u}) \in \mathbb{R}^{p^2 \times f}$; where p and f determine the patch size and the number of features. In Eq. (2), we seek the dictionary D of c atoms and corresponding sparse code A to represent $S_p(\tilde{u})$, solving the following ρ -regularized dictionary learning problem:

$$\begin{aligned} \min_{D, A} \|S_p(\tilde{u}) - DA\|_F^2 + \rho \|A\|_F^2 \\ \text{subject to } \|d_j\|_2 = 1, j = 1, \dots, c \\ \|a_l\|_0 \leq L, l = 1, \dots, f. \end{aligned} \quad (2)$$

A couple of optimized D and A is obtain through regularized K-SVD training iterations. With the final fixed D , the ultimate sparse code A is then found using the orthogonal matching pursuit (OMP) algorithm with $\lfloor \frac{p^2}{10} \rfloor$ transforming sparsity to reconstruct the denoised observed data $\hat{u} = S_p^{-1}(DA)$ from the patches, via the inverse S_p^{-1} . $\|\cdot\|_F$ is the Frobenius matrix norm. We define $\mathcal{G}_{\hat{u}}(x_i, t_j) = \hat{u}_{ij}$ as the denoised state function.

If we encounter 3D or 4D spatial-temporal data, denoised \hat{u} is achieved efficiently by applying 2D Savitzky-Golay filters (Ratzlaff and Johnson 1989; Krumm 2001), which can be used with SVD (singular value decomposition).

PDE Identification

Best-subset regression is used next to recover a sequence of potential parsimonious PDEs along their corresponding coefficients, with a maximal bound of support sizes (i.e., the number of nonzero coefficients). Basically, a careful forward-backward elimination algorithm (Guyon et al. 2002) can be implemented to approximate the best subsets.

We compute a presumably overcomplete (with a maximum derivative order) library $\Phi(\hat{u})$, collecting candidate terms of the denoised observed data. According to the weak formulation (Reinhold, Gurevich, and Grigoriev 2020), i -th numerical value of j -th candidate (column-wise) in $\Phi(\hat{u}) \in \mathbb{R}^{N_\Omega \times N_q}$ is given by integrating over a local spatio-temporal subdomain Ω_i , whose (rectangular) lengths are H_x and H_t .

$$\Phi(\hat{u}) = [\cdots \quad q_j \quad \cdots], \quad j = 1, \dots, N_q; \quad (3)$$

$$q_j^i = \int_{\Omega_i} w \phi_j d\Omega, \quad i = 1, \dots, N_\Omega.$$

ϕ_j is regarded as a candidate function, for example, $\mathcal{G}_{\hat{u}}^2$ and $\partial_x^2 \mathcal{G}_{\hat{u}}$. N_Ω is the number of domain centers; $\forall i, (x_i^c, t_i^c)$. The smooth weight, e.g., $w = (x^2 - 1)^2 (t^2 - 1)^2$; where $x = (x - x_i^c)/H_x, t = (t - t_i^c)/H_t$ conditioned by $(x, t) \in [-1, 1]^2$, is a viable function for discovering the Burgers' PDE as it vanishes along the boundary $\partial\Omega_i$. Certainly, higher polynomial orders are possible. By integration by parts on Eq. (3), numerical noisy derivative evaluation of ϕ_j is supposed to be carried out on the noiseless w . We use the implementation provided in the PySINDy package (de Silva et al. 2020; Kaptanoglu et al. 2022). Remark that the noise-tolerant representation by the convolutional weak formulation (CWF) (Messenger and Bortz 2021) could be leveraged at the library construction stage as well.

We attain an estimate $\hat{\xi}^k$ of the optimal PDE coefficients with s_k support sizes by the best-subset selection:

$$\hat{\xi}^k = \arg \min_{\xi^k} \left\| q_0 - \sum_{j=1}^{N_q} q_j \xi_j^k \right\|_2^2, \quad \text{subject to } \|\xi^k\|_0 = s_k; \quad (4)$$

where $q_0^i = \int_{\Omega_i} w \partial_t \mathcal{G}_{\hat{u}} d\Omega$, and $q_0 \approx \sum_{j=1}^{N_q} q_j \xi_j^k = \Phi(\hat{u}) \xi^k$. Best-subset solvers, we experiment with to yield potential PDEs for an increasing sequence of support sizes $(s_k)_{k=1}^{N_s}$, are based on MIO, SOS-1-formulated (type-1 specially ordered sets) (Bertsimas and Weismantel 2005) MIO-SINDy, FROLS (forward regression with orthogonal least squares) (Chen, Billings, and Luo 1989; Billings 2013) and LOBnB (branch-and-bound framework for sparse regression) (Hazimeh, Mazumder, and Saab 2021).

Uncertainty-penalized Bayesian Information Criterion (UBIC) for Adaptive Model Selection

This section finds the best number of supports presented in Eq. (4) within a given range. The base metric, on which we rely to penalize the maximized log-likelihood value of a regression model with its complexity, is the BIC:

$$\text{BIC}(\hat{\xi}^k) = -2 \log L(\hat{\xi}^k) + \log(N_\Omega) s_k; \quad (5)$$

$$\log L(\hat{\xi}^k) = -\frac{N_\Omega}{2} \log \left(\frac{2\pi}{N_\Omega} \left\| q_0 - \Phi(\hat{u}) \hat{\xi}^k \right\|_2^2 \right).$$

L is the model likelihood. Assuming the true governing PDE is parameterized by the vector-valued coefficient that distributes with relatively less uncertainty, compared to those that build the other potential PDEs, we define the UBIC as

$$\text{UBIC}(\xi^k, \lambda_U) = \text{BIC}(\xi_\mu^k) + \lambda_U \log(N_\Omega) U^k$$

$$= -2 \log L(\xi_\mu^k) + \log(N_\Omega) (s_k + \lambda_U U^k), \quad (6)$$

where U^k represents an estimated total uncertainty for ξ^k , scaled proportionally to $\log(N_\Omega)$, similar to the penalizing complexity in the BIC, for convenient unification. The data-dependent λ_U controlling influence of U^k on model selection is adaptively adjusted by Algorithm 1. Typically, a lower UBIC means a better-discovered PDE. Bayesian linear regression probabilistic view is placed on ξ^k with Gaussian conjugate prior $\mathcal{N}(\xi^k | \xi_0^k, V_0^k)$ to setup the posterior:

$$p(\xi^k | \Phi(\hat{u}), q_0, \sigma_q) \sim \mathcal{N}(\xi^k | \xi_0^k, V_0^k) \mathcal{N}(q_0 | \Phi(\hat{u}) \xi^k, \sigma_q^2 \mathbf{I}_{N_\Omega})$$

$$= \mathcal{N}(\xi^k | \xi_\mu^k, V^k);$$

$$\xi_\mu^k = V^k (V_0^k)^{-1} \xi_0^k + \frac{1}{\sigma_q^2} V^k \Phi(\hat{u})^T q_0,$$

$$V^k = \sigma_q^2 (\sigma_q^2 (V_0^k)^{-1} + \Phi(\hat{u})^T \Phi(\hat{u}))^{-1}. \quad (7)$$

Later presented experimental results are produced with $\xi_0^k = \hat{\xi}^k$ and $V_0^k = \mathbf{I}_{\|\hat{\xi}^k\|_0}$ as an identity matrix of size $\|\hat{\xi}^k\|_0$. Note that $\xi_0^k = \vec{0}$, reducing the posterior mean to ridge estimate, is also a feasible option. By maximum likelihood estimation (MLE), we accordingly set the error variance $\sigma_q^2 = \mathbb{E}[(q_0 - \Phi(\hat{u}) \hat{\xi}^k)^2]$. Inspired by the coefficient of variation formula, the uncertainty U^k is defined as

$$U^k = \frac{\text{CV}^k}{\min_k \text{CV}^k}; \quad \text{CV}^k = \frac{\left\| \text{diag}(V^k)^{\circ \frac{1}{2}} \right\|_1}{\|\xi_\mu^k\|_1} = \frac{\sum_{i=j}^{s_k} \sqrt{V_{ij}^k}}{\|\xi_\mu^k\|_1}. \quad (8)$$

Here we essentially compute the relative standard deviation of the covariance matrix V^k by taking an element-wise square (the $\circ \frac{1}{2}$ exponent) root on its diagonal vector (diag) and then the division by $\|\xi_\mu^k\|_1$. Each CV^k is rescaled by its minimum respecting the range of available support sizes, resulting in U^k whose numerical value is comparable to s_k .

Once U^k is obtained, we converge the UBIC by Algorithm 1, iteratively decreasing λ_U from its maximum bound λ_U^{\max} derived to maintain the influence of the log-likelihood value (presumably greater than zero) in Eq. (6). We impose the constraint based on the discovered s_k -support PDE.

$$\log N_\Omega (s_k + \lambda_U U^k) \leq \left| -2 \log \hat{L}(\xi_\mu^k) \right|; \quad \lambda_U \geq 0$$

$$0 \leq \lambda_U \leq \lambda_U^{\max} = \max_k \frac{1}{U^k} \left(\frac{2 \log \hat{L}(\xi_\mu^k)}{\log N_\Omega} - s_k \right) \quad (9)$$

Algorithm 1 finds a proper $\lambda_U = 10^\lambda$ by reducing λ iteratively. We track the current and competitive optimal support sizes (s_{k^*}, s_{k^c}) , and test the terminate condition at line 12, which essentially checks whether we have the increased complexity with unsatisfactory improvement (see τ), or the

Algorithm 1: Find the optimal complexity s_{k^*} by tuning λ_U

Input: $\Phi(\hat{u})$, q_0 and $\hat{\xi}^k$

Parameter: τ_0 : Improvement acceptance threshold (default = 0.02), $N_\delta = 3$: Number of evenly spaces in $[0, \log_{10} \lambda_U^{\max}]$

Output: The optimal support sizes s_k^* and tuned UBIC's hyperparameter λ_U

- 1: Compute $\forall k \leq N_s$, V^k , ξ_μ^k and U^k ,
with Gaussian prior $\mathcal{N}(\xi^k | \hat{\xi}^k, \mathbf{I}_{\|\hat{\xi}^k\|_0})$
 - 2: Assign $\lambda \leftarrow \log_{10} \max(\lambda_U^{\max}, 0)$ $\{-\infty$ if $\lambda_U^{\max} < 0\}$
 - 3: Assign $\delta \leftarrow \frac{\lambda}{N_\delta}$ and $\lambda^c \leftarrow \lambda - \delta$ {next candidate for λ }
 - 4: Compute $\forall k$, $\mathcal{I}_k \leftarrow \text{UBIC}(\xi^k, 10^\lambda)$ using ξ_μ^k and U^k
 - 5: Find s_{k^*} where $k^* \leftarrow \arg \min_k \mathcal{I}_k$
 - 6: **while** $\lambda^c > 0$ **do**
 - 7: Compute $\forall k$, $\mathcal{I}_k^c \leftarrow \text{UBIC}(\xi^k, 10^{\lambda^c})$
 - 8: Find s_{k^c} where $k^c \leftarrow \arg \min_k \mathcal{I}_k^c$
 - 9: Assign $\Delta s \leftarrow s_{k^c} - s_{k^*}$
 - 10: Assign $\Delta \text{BIC} \leftarrow \text{BIC}(\xi_\mu^{k^c}) - \text{BIC}(\xi_\mu^{k^*})$
 - 11: Assign $\tau \leftarrow \tau_{k^*}^{k^c}$; $\tau_{k^*}^{k^c} = |\Delta \text{BIC} / (\text{BIC}(\xi_\mu^{k^*}) \Delta s)|$
 - 12: **if** ($\Delta s > 0$ but ($\Delta \text{BIC} > 0$ or $\tau < \tau_0$)) or
 ($\Delta s < 0$ but $\Delta \text{BIC} > 0$ and $\tau > \tau_0$) **then**
 - 13: **break** {terminate condition detected}
 - 14: **end if**
 - 15: Assign $\lambda \leftarrow \lambda^c$ and $\lambda^c \leftarrow \lambda - \delta$
 - 16: Assign $\forall k$, $\mathcal{I}_k \leftarrow \mathcal{I}_k^c$ and $k^* \leftarrow k^c$ $\{s_{k^*} \leftarrow s_{k^c}\}$
 - 17: **end while**
 - 18: **if** $|\text{BIC}(\xi_\mu^{k^*}) - \text{BIC}(\xi_\mu^{k^* - 1})| / |\text{BIC}(\xi_\mu^{k^* - 1})| < \tau_0$ **then**
 - 19: Consider an increased τ_0 to prevent overfitting
 - 20: **end if**
 - 21: **return** s_{k^*} , $\lambda_U = 10^\lambda$ and $\forall k$, \mathcal{I}_k {used in plotting}
-

decreased complexity with already satisfying improvement. Also, τ_0 can be set adaptively, yet offering the same correct selection as the default value. Such an effective heuristic is $\tau_0 = P_{75}(S)$; $S = \{\tau_{k^1}^{k^2} \mid k^1, k^2 = \arg \min(r) \text{ s.t. } r = s_{k^2} - s_{k^1} > 0, \text{ and } \forall s_{k^0} < s_{k^1}, \text{BIC}(\xi_\mu^{k^2}) < \text{BIC}(\xi_\mu^{k^1}) < \text{BIC}(\xi_\mu^{k^0})\}$, the 75th percentile of successive improvement factors respecting just BIC-decreasing models. If an overfitted model is detected by line 18, we retry with a stricter percentile of S , e.g., $P_{80}(S)$. Contrarily, lessening τ_0 helps discern selecting a supposedly underfitted 1-support PDE.

Simulation-based Model Selection

As Eq. (4) optimizes for the regression model that fits $\Phi(\hat{u})$ to approximate q_0 (a weak form of u_t), the attained model do not offer the direct comparison metric to the PDE solution u . However, they are expected to yield the true PDE, reducing unnecessary costs of simulating false governing PDEs.

As an aid validation process, which can be computationally expensive or numerically infeasible for some ill-posed PDEs, we solve the found PDEs most likely to be the true PDE form based on our UBIC scores. Well-known numerical PDE solvers based on spectral methods are available in Chebfun (Battles and Trefethen 2004) and Dedalus (Burns et al. 2020). The software can accurately solve canonical

stiff PDEs given initial and boundary conditions. Nevertheless, when solving a PDE containing extraneous high-order derivatives, the simulated solution may explode over time. Mathematical analysis is needed to rigorously address ill-posed PDEs, characterized by numerical instability in their solutions. Though such analysis exceeds our scope, we give the flexible neural network based treatise.

Physics-informed Neural Network (PINN) Learning

PINN learning is an alternative approach for solving PDEs. The learned solution not only satisfies a specified PDE but is also stabilized to fit observational data. The general principle is to learn the mapping function from spatio-temporal data (in $\mathcal{D} = \{(x_i^D, t_j^D)\}$ split) to denoised s_k -support PDE solution: $\forall i, j : (x_i^D, t_j^D) \xrightarrow{f_{\Theta_k}} \hat{u}_{ij}^D$ by minimizing the physics-informed loss respecting the discovered function $\hat{\mathcal{N}}$.

$$\Theta_k^* = \arg \min_{\Theta_k} \left(\|\mathcal{F}_{\Theta_k}^D - \hat{u}^D\|_F^2 + \left\| \partial_t \mathcal{F}_{\Theta_k}^D - \hat{\mathcal{N}}(\mathcal{F}_{\Theta_k}^D, \partial_x \mathcal{F}_{\Theta_k}^D, \partial_x^2 \mathcal{F}_{\Theta_k}^D, \dots; \hat{\xi}^k) \right\|_F^2 \right) \quad (10)$$

We collect $(\mathcal{F}_{\Theta_k}^D)_{ij} = f_{\Theta_k}(x_i^D, t_j^D)$. $\mathcal{D}_{\text{Train}}$ is the train split containing subsampled discretized spatio-temporal points, on which the PINN is trained, and likewise \mathcal{D}_{Val} for hold-out validation dataset. Automatic differentiation is used to compute derivative terms, e.g., $\partial_x \mathcal{F}_{\Theta_k}^D$. Θ_k is optimized by the second-order LBFGS (Liu and Nocedal 1989). Trainable $\hat{\xi}^k$ is initialized beforehand from Eq. (4).

Deciding whether the s_k -support PDE is better or worse than the s_{k+1} -support PDE, we adjust the BIC in Eq. (5) as the complexity penalization avoids choosing the overfitted PDE that also generate the PINN predicted solution close to $\hat{u}^{\mathcal{D}_{\text{Val}}}$ on the validation split. The state-level BIC reads

$$\text{BIC}_{\Theta_k^*}^{\hat{u}}(\hat{\xi}^k) = -|\mathcal{D}_{\text{Val}}| \log \left(\frac{2\pi}{|\mathcal{D}_{\text{Val}}|} \left\| \hat{u}^{\mathcal{D}_{\text{Val}}} - \mathcal{F}_{\Theta_k^*}^{\mathcal{D}_{\text{Val}}} \right\|_F^2 \right) + \log(|\mathcal{D}_{\text{Val}}|) (|\Theta_k^*| + \|\hat{\xi}^k\|_0); \quad (11)$$

where $|\Theta_k^*|$ tells the network's number of trainable parameters. The modification involves utilizing the validation data points in \mathcal{D}_{Val} for the comparison. If $\text{BIC}_{\Theta_k^*}^{\hat{u}}(\hat{\xi}^k) < \text{BIC}_{\Theta_{k+1}^*}^{\hat{u}}(\hat{\xi}^{k+1})$, it is advisable not to increase the support sizes to s_{k+1} under a fair circumstance where the PINN architecture and learning procedure are identical. We adhere to the vanilla paradigm for simplicity, though the PINN training could be improved, e.g., using multi-task learning techniques (Thanasutives, Numao, and Fukui 2021), since the network may overfit on $\mathcal{D}_{\text{Train}}$, stuck in a physics-obeying local minimum (Bajaj et al. 2023).

Numerical Result

The PDE dataset description is given in Table 1. Experiments were run on a 2.6 GHz 6-Core Intel i7 CPU with 32 GB RAM. Further results and analysis are in the supplement.

Table 1: PDE descriptions. The number of discretized spatial and temporal points are specified by the (N_x, N_y, N_z) and N_t .

Dataset	PDE	N_x, N_y, N_z	N_t	ϵ
Burgers	$\partial_t u = 0.1 \partial_x^2 u - u \partial_x u$	256 on $[-8, 8]$	101 on $[0, 10]$	30
KdV	$\partial_t u = -\partial_x^3 u - u \partial_x u$	512 on $[-20, 20]$	501 on $[0, 40]$	30
KS	$\partial_t u = -\partial_x^2 u - \partial_x^4 u - u \partial_x u$	1024 on $[0, 32\pi]$	251 on $[0, 100]$	30
NS	$w_t = 0.01(w_{xx} + w_{yy}) - uw_x - vw_y$	325×170 on $[2, 8.48] \times [0.3, 3.68]$	151 on $[0, 30]$	1
RD	$u_t = u - u^3 + v^3 - uv^2 + u^2v + 0.1(u_{xx} + u_{yy})$ $v_t = v - u^3 - v^3 - uv^2 - u^2v + 0.1(v_{xx} + v_{yy})$	256×256 on $[-10, 10] \times [-10, 10]$	201 on $[0, 10]$	10
GS	$u_t = 0.014 - 0.014u - uv^2 + 0.02(u_{xx} + u_{yy} + u_{zz})$ $v_t = -0.067v + uv^2 + 0.01(v_{xx} + v_{yy} + v_{zz})$	$128 \times 128 \times 128$ on $[-1.25, 1.25]^3$	100 on $[0, 10]$	0.1

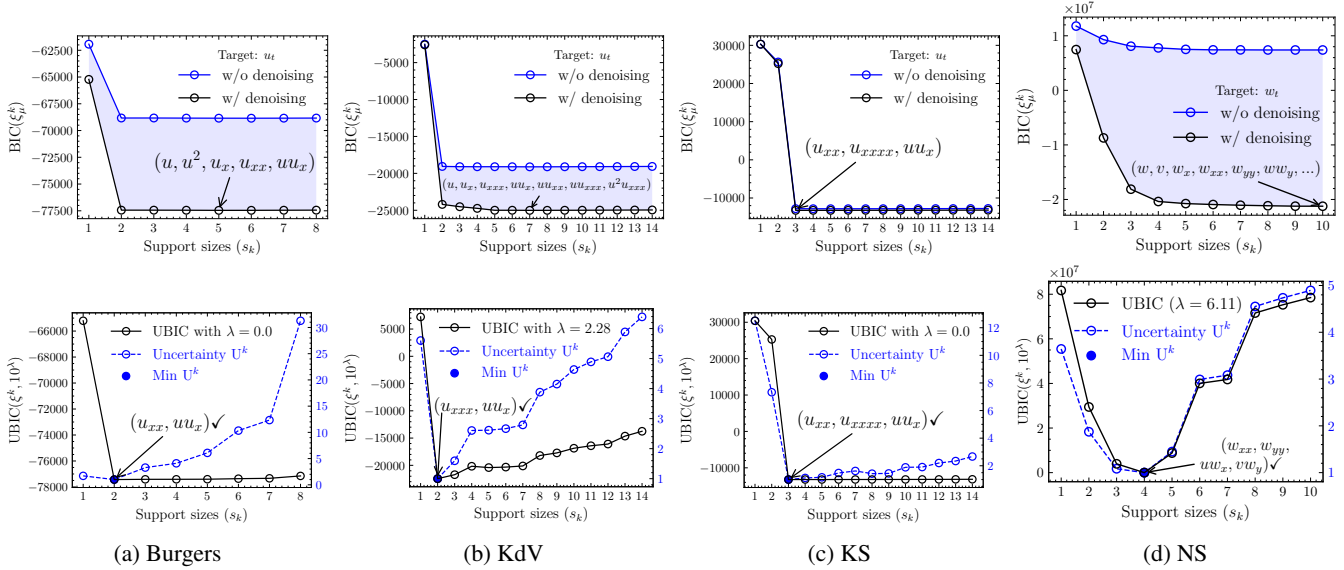


Figure 2: We plot the BIC, uncertainty U^k and UBIC with tuned $\lambda_U = 10^\lambda$ for the model selection in the Burgers, KdV, KS, and NS examples, arranged from left to right. “ \checkmark ” indicates that the UBIC selects the true PDE form.

Burgers’ PDE We tested the PDE solution with the initial condition: $u(x, 0) = e^{-(x+2)^2}$. To denoise \tilde{u} , we ran regularized KSVD with $\rho = 0.05$ on the stack $S_p(\tilde{u})$ created with square patches of size 8×8 . For sparse encoding during the training, OMP was configured with one target sparsity.

We gathered an overcomplete set of candidate functions $\phi_j(\cdot) \in \{(\mathcal{G}_{\tilde{u}}^{d_1} \partial_x^{d_2} \mathcal{G}_{\tilde{u}})(\cdot) \mid d_1 + d_2 \geq 1; d_1, d_2 = 0, 1, 2\}$ for transforming to the integral weak forms, $(\Phi(\hat{u}), q_0)$. Exhaustive all subsets selection solved Eq. (4), attaining $\hat{\xi}^k$ for every $k \leq N_q = 8$ (an constant intercept or bias excluded).

Figure 2a (top) shows the BIC scores of the found PDEs, where the support sizes are arranged in increasing order. After the 2-support PDE, the improvement in BIC becomes stagnant. However, the model selection based on BIC would not choose the 2-support PDE as the optimal choice. This is because the scores continue decreasing beyond the plateau in the BIC scores, and the 5-support PDE actually yields the lowest BIC score. We inspect that the log-likelihood dominates the BIC score, when the number of samples in the library N_Ω is large. The evidence reveals the impropriety of using the BIC for identifying the true governing PDE.

To leverage the proposed UBIC, we quantify the uncertainty U^k from all the best subsets, as plotted in Figure 2a. The PDE with 2 support sizes exhibits the highest stability. These uncertainties are incorporated to penalize the previously obtained BIC scores, preferring the parsimonious PDE with the reliable coefficient estimates. Algorithm 1 suggests the UBIC scores with $\lambda_U = 10^0 = 1$. As a result, the selected PDE aligns with the true Burgers’ PDE form.

Korteweg–De Vries (KdV) PDE We generated the two-soliton u with the initial condition $u(x, 0) = -\sin(\frac{\pi x}{20})$. We employed denoising regularized KSVD with $\rho = 0.01$ on the stack $S_p(\tilde{u})$ created with 25×25 patches. We set the OMP algorithm with one target sparsity during the training.

Next, the candidate functions $\phi_j(\cdot)$ were chosen from $\{(\mathcal{G}_{\tilde{u}}^{d_1} \partial_x^{d_2} \mathcal{G}_{\tilde{u}})(\cdot) \mid d_1 + d_2 \geq 1; d_1 = 0, 1, 2 \text{ and } d_2 = 0, 1, 2, 3, 4\}$ before building their weak forms and q_0 . We exhaustively searched for all the optimal subsets respecting every number of supports, achieving $\forall k \leq N_q = 14, \hat{\xi}^k$.

In Figure 2b, we observe that the true equation favored by the UBIC with tuned $\lambda_U = 10^{2.28}$ stands out, in accordance with the minimal uncertainty, than the other potential PDEs.

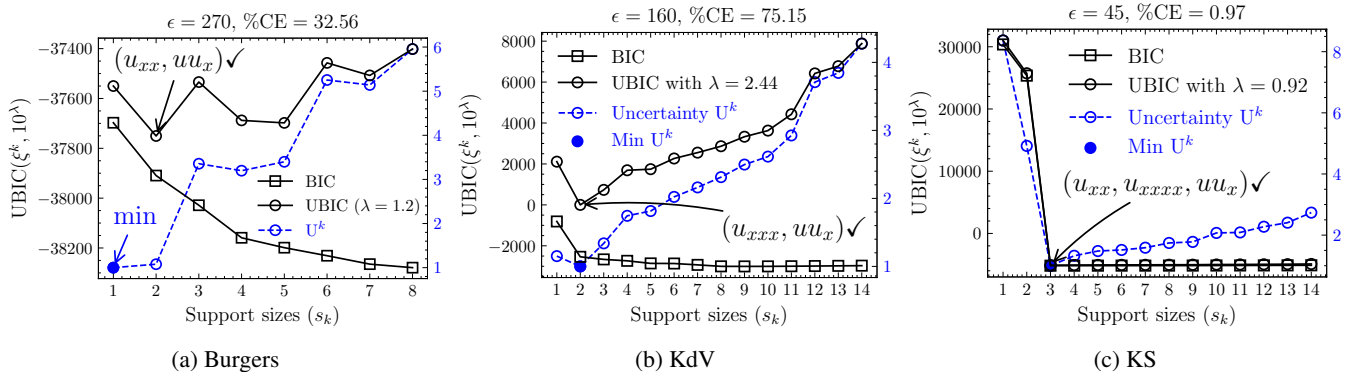


Figure 3: Robust adaptive model selection by the UBIC under the extremely noisy scenarios.

Table 2: The better is underlined (%CE) or on **bold** (R_{BIC}).

Dataset	w/o Denoising		w/ Denoising	
	%CE	R_{BIC}	%CE	R_{BIC}
Burgers	0.7900	-6919	0.9108	-12236
KdV	17.34	-16614	<u>9.2987</u>	-22419
KS	0.4508	-43121	<u>0.3813</u>	-43533
NS	False Eq.	-4379570	<u>11.43</u>	-28710947
RD: u_t	3.1177	-14790	<u>2.1639</u>	-14963
RD: v_t	3.3251	-15729	<u>2.2967</u>	-15916
GS: u_t	<u>0.02621</u>	-106720	0.05542	-113852
GS: v_t	0.01108	-114432	<u>0.01096</u>	-120588

Kuramoto–Sivashinsky (KS) PDE Following the PDE-FIND paper (Rudy et al. 2017), we experimented with the identical chaotic PDE generated with the initial condition: $u(x, 0) = \cos(\frac{x}{16})(1 + \sin(\frac{x}{16}))$. We used the same regularized KSVD settings as detailed in the KdV example.

Since the set of candidate functions adopted in the KdV example was sufficient to build an overcomplete weak form library for recovering the KS PDE, we underwent the same best-subset regression strategy.

As shown in Figure 2c, the lowest BIC and UBIC score with just $\lambda_U = 1$ offer the desirable outcome, pointing to the true equation form.

Navier-Stokes (NS) PDE We consider the explicit form of the NS equation given in the 3D spatial-temporal grid. As seen in Table 1, w denotes the vorticity. The components of the velocity field are denoted by u (x -component) and v (y -component), which are both treated as known terms to construct an overcomplete library. We generated the dataset according to the instructions given in the PDE-FIND paper and focused on the bounded spatial domain $(x, y) \in [2, 8.48] \times [0.3, 3.68]$ after the cylinder. We were left with, in total 8,342,750 data points, for each variable: w, u, v , to which 1%-sd noise was added after the subsampling.

To obtain each noise-reduced variable, we applied 2D Savitzky-Golay filters along the temporal axis and then employed the denoising SVD. As experimented in the PDE-FIND, we specifically retained the top singular values, which were 26, 20, and 20 for w, u , and v (reshaped as met-

rics with 325×170 rows and 151 columns), respectively. The process enhanced the variables' quality, thereby preserving the correct equation form to be captured at the discovered 4-support PDE. There were 19 non-weak terms listed from the variables: $\psi_1 \in \{w, u, v\}$, the spatial derivatives of the vorticity w : $\psi_2 \in \{w_x, w_{xx}, w_y, w_{yy}\}$ or the interactions $\psi_1\psi_2$. Every best subset, whose cardinality ranges from 1 to 10 is initially approximated by the MIQP (mixed-integer quadratic programming) with the L0-norm based budget constraint (Bertsimas, King, and Mazumder 2016). Then we carried out an all-subsets exhaustive search over the top candidates, each at least existing in one of the 10 best subsets.

Despite the underlying PDE form being dependent on the 4 supports, it is the most stable one, as illustrated in Figure 2d (bottom). Undoubtedly, the quantified uncertainty associated with each discovered PDE is a beneficial factor for finding the correct model by the UBIC with $\lambda_U = 10^{6.11}$.

Denoising Effect The positive effect of denoising is clearly evident from the major drop in BIC, observed throughout the previously studied examples. We measure the improvement by the maximum reduction in the BIC: $R_{\text{BIC}} = \min_k \text{BIC}(\hat{\xi}_\mu^k) - \max_k \text{BIC}(\hat{\xi}_\mu^k)$ in Table 2. In Figure 2c, the reduction in BIC scores is not as pronounced as what is demonstrated in the Burgers and KdV examples, implying the challenge of restoring the chaotic pattern of the KS PDE. Meanwhile, in the NS example, the omission of the true PDE when no denoising processes were performed causes the noticeable gap in the BIC values between the two cases, as illustrated in Figure 2d, confirming the usefulness of the denoising step to the model selection. R_{BIC} or generally the area between trade-offs is a prospective metric for tuning denoising hyperparameters.

Robust Adaptive Model Selection We fully harness the capability of our proposed method in such extremely noisy scenarios that, without the denoising step, the true governing PDE would be omitted or poorly recovered from the potential best subsets. As visualized in Figure 3, we correctly identify the governing PDEs selected using the adaptive UBIC despite the severe noise interference. Particularly noteworthy is the Burgers example, where neither the BIC nor the uncertainty alone can recover the true equation form.

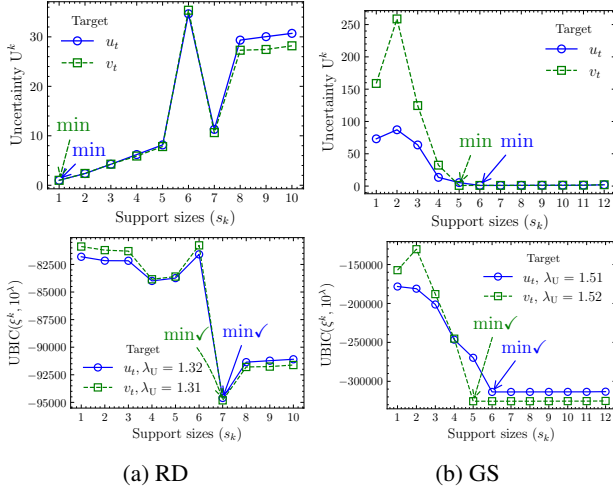


Figure 4: Model selection results for the RD and GS PDEs.

Discovery Accuracy We evaluate the proximity between the discovered $\hat{\xi}_j^k$ and ground truth ξ_j by the %CE (percentage coefficient error): $100 \times \left| \frac{\hat{\xi}_j^k - \xi_j}{|\xi_j|} \right|$. The average over every effective coefficient is reported in Table 2 for each dataset in Table 1. $\hat{\xi}^k$ obtained on the denoised data delivers the lower average %CE than the case without denoising.

Reaction-Diffusion (RD) PDE The PDE governs a system that simulates double spiral waves on a periodic domain, consisting of 7 actual terms. To countermeasure 10% noise that perturbed a stack of the u and v variables, 2D Savitzky-Golay filters were employed along the temporal axis, the results were then collected to construct the noise-reduced data.

The candidates were chosen from the variables and their transformations: $\psi_1 \in \{u, v, u^3, v^3, u^2v, uv^2\}$, the spatial derivatives (up to second-order) of either u or v : $\psi_2 \in \{u_x, u_y, u_{xx}, u_{yy}, u_{xy}, v_x, v_y, v_{xx}, v_{yy}, v_{xy}\}$, or possible interactions $\psi_1\psi_2$. To identify the best subset for each cardinality from 1 to 10, an initial approximation was obtained using the MIQP with the budget constraint based on the L0-norm. Subsequently, we validated and ensured the optimality of the subsets, whose support sizes were not greater than 10, respecting the set of unique effective candidates.

Figure 4a shows that the uncertainty alone is not enough for the model selection as it positively correlated with the number of supports, signifying the necessity of the base BIC in Eq. (6). The single-support PDE exhibits the least uncertainty. However, an intriguing observation emerges at the 7-support PDE, where the uncertainty drops relatively to the surrounding PDEs plotted alongside. The stability is effectively exploited by the tuned UBIC with $\lambda \approx 1.31$ to successfully identify the true 7 candidates.

Gray-Scott (GS) PDE The GS PDE models the reaction-diffusion system in the 4D spatial-temporal grid. We looped over the stack of the variables along the t -temporal then z -spatial axes to mitigate the noise effect by 2D Savitzky-

Table 3: PINN-based model selection between the PDEs with (optimal) s_{k^*} and (sub-optimal) s_{k^*+1} support sizes.

Support sizes	Burgers	KdV	KS
s_{k^*}	-16439(2) ¹	247070(2)	339036(3)
s_{k^*+1}	-2020(3)	280799(3)	501440(4)

¹The support sizes are denoted in parentheses.

Golay filters. Hereafter, similarly to the NS example, each variable was reconstructed via the denoising SVD, retaining the 10 most significant singular values.

We comprised an overcomplete candidate library with the variables (including an intercept) and their transformations: $\{1, u, v, u^3, v^3, u^2v, uv^2\}$, the spatial derivatives of u : $\{u_x, u_y, u_z, u_{xx}, u_{yy}, u_{zz}, u_{xy}, u_{xz}, u_{yz}\}$, and the spatial derivatives of v : $\{v_x, v_y, v_z, v_{xx}, v_{yy}, v_{zz}, v_{xy}, v_{xz}, v_{yz}\}$. The approximated best subsets were retrieved using the FROLS solver with a maximum support size of 12. These subsets were guaranteed to be at their optimum within all the effective candidates, each once delivered by the solver.

According to Figure 4b, it is evident that the best subsets, which align with the true complexity of the PDE system with support sizes of 6 and 5 for the targets u_t and v_t , exhibit the minimal uncertainties. The tuned UBIC ($\lambda \approx 1.51$) leverages the uncertainty pattern to penalize the BIC values, hence the successful identification of the true PDE system.

Simulation-based Model Comparison We simulated the PDE selected by the tuned UBIC and another PDE with an additional candidate, using the PINN learning. Comparing the two PDEs, we measured the proximity of their simulated solutions to the denoised version of the observed state variable using the BIC in Eq. (11). Table 3 warrants that the s_{k^*} -support PDE has indeed the sufficient complexity in yielding the lower-BIC simulated state variable than its competitor, the s_{k^*+1} -support PDE with the extra candidate.

Conclusion

We extend the BIC to the parameter-adaptive UBIC, which incorporates the model uncertainty for selecting the governing PDE amidst noisy data. The uncertainty, quantified from the model coefficient posterior, promotes the reliability into the model selection, preventing the rise of overfitted PDEs unaddressed by the BIC. The proposed UBIC demonstrates the successful identification of the true hidden equation while maintaining computational efficiency thanks to the analytical posterior form. Validating consistency in model selection results, we perform a comparison between the PDE selected by the UBIC and its competitor with an extra support to find the better PDE that delivers a lower BIC value calculated between the simulated state and the denoised observed data. Notably, the discovery on denoised data positively improves the BIC trade-off. Towards more complicated examples, we will explore applying the UBIC to the evolutionary-based discovery methods (Xu, Chang, and Zhang 2020) to relax the overcompleteness assumption.

References

- Akaike, H. 1974. A new look at the statistical model identification. *IEEE Transactions on Automatic Control*, 19(6): 716–723.
- Bajaj, C.; McLennan, L.; Andeen, T.; and Roy, A. 2023. Recipes for when physics fails: recovering robust learning of physics informed neural networks. *Machine Learning: Science and Technology*, 4(1): 015013.
- Battles, Z.; and Trefethen, L. N. 2004. An Extension of MATLAB to Continuous Functions and Operators. *SIAM Journal on Scientific Computing*, 25(5): 1743–1770.
- Bertsimas, D.; and Gurnee, W. 2023. Learning sparse nonlinear dynamics via mixed-integer optimization. *Nonlinear Dynamics*, 111(7): 6585–6604.
- Bertsimas, D.; King, A.; and Mazumder, R. 2016. Best subset selection via a modern optimization lens. *The Annals of Statistics*, 44(2): 813 – 852.
- Bertsimas, D.; and Weismantel, R. 2005. *Optimization Over Integers*. Dynamic Ideas.
- Billings, S. A. 2013. *Nonlinear system identification: NARMAX methods in the time, frequency, and spatio-temporal domains*. John Wiley & Sons.
- Brunton, S. L.; Proctor, J. L.; and Kutz, J. N. 2016. Discovering governing equations from data by sparse identification of nonlinear dynamical systems. *Proceedings of the national academy of sciences*, 113(15): 3932–3937.
- Burns, K. J.; Vasil, G. M.; Oishi, J. S.; Lecoanet, D.; and Brown, B. P. 2020. Dedalus: A flexible framework for numerical simulations with spectral methods. *Phys. Rev. Res.*, 2: 023068.
- Chen, S.; Billings, S. A.; and Luo, W. 1989. Orthogonal least squares methods and their application to non-linear system identification. *International Journal of control*, 50(5): 1873–1896.
- Cranmer, M. 2023. Interpretable Machine Learning for Science with PySR and SymbolicRegression.jl. arXiv:2305.01582.
- de Silva, B.; Champion, K.; Quade, M.; Loiseau, J.-C.; Kutz, J.; and Brunton, S. 2020. PySINDy: A Python package for the sparse identification of nonlinear dynamical systems from data. *Journal of Open Source Software*, 5(49): 2104.
- Dong, X.; Bai, Y.-L.; Lu, Y.; and Fan, M. 2023. An improved sparse identification of nonlinear dynamics with Akaike information criterion and group sparsity. *Nonlinear Dynamics*, 111(2): 1485–1510.
- Dumitrescu, B.; and Irofti, P. 2017. Regularized K-SVD. *IEEE Signal Processing Letters*, 24(3): 309–313.
- Faul, A.; and Tipping, M. 2001. Analysis of Sparse Bayesian Learning. In Dietterich, T.; Becker, S.; and Ghahramani, Z., eds., *Advances in Neural Information Processing Systems*, volume 14. MIT Press.
- Guyon, I.; Weston, J.; Barnhill, S.; and Vapnik, V. 2002. Gene selection for cancer classification using support vector machines. *Machine learning*, 46(1): 389–422.
- Hazimeh, H.; Mazumder, R.; and Saab, A. 2021. Sparse regression at scale: Branch-and-bound rooted in first-order optimization. *Mathematical Programming*, 1–42.
- Hirsh, S. M.; Barajas-Solano, D. A.; and Kutz, J. N. 2022. Sparsifying priors for Bayesian uncertainty quantification in model discovery. *Royal Society Open Science*, 9(2): 211823.
- Horrocks, J.; and Bauch, C. T. 2020. Algorithmic discovery of dynamic models from infectious disease data. *Scientific Reports*, 10(1): 7061.
- Ishwaran, H.; and Rao, J. S. 2005. Spike and slab variable selection: Frequentist and Bayesian strategies. *The Annals of Statistics*, 33(2).
- Kaptanoglu, A. A.; de Silva, B. M.; Fasel, U.; Kaheman, K.; Goldschmidt, A. J.; Callahan, J.; Delahunt, C. B.; Nicolaou, Z. G.; Champion, K.; Loiseau, J.-C.; Kutz, J. N.; and Brunton, S. L. 2022. PySINDy: A comprehensive Python package for robust sparse system identification. *Journal of Open Source Software*, 7(69): 3994.
- Krumm, J. 2001. Savitzky-Golay filters for 2D images. *Microsoft Research, Microsoft Corporation, Redmond, WA*.
- Lagergren, J. H.; Nardini, J. T.; Michael Lavigne, G.; Rutter, E. M.; and Flores, K. B. 2020. Learning partial differential equations for biological transport models from noisy spatio-temporal data. *Proceedings of the Royal Society A: Mathematical, Physical and Engineering Sciences*, 476(2234): 20190800.
- Li, J.; Sun, G.; Zhao, G.; and Li-wei, H. L. 2020. Robust low-rank discovery of data-driven partial differential equations. In *Proceedings of the AAAI Conference on Artificial Intelligence*, volume 34, 767–774.
- Li, S.; Kaiser, E.; Laima, S.; Li, H.; Brunton, S. L.; and Kutz, J. N. 2019. Discovering time-varying aerodynamics of a prototype bridge by sparse identification of nonlinear dynamical systems. *Phys. Rev. E*, 100: 022220.
- Liu, D. C.; and Nocedal, J. 1989. On the limited memory BFGS method for large scale optimization. *Mathematical programming*, 45(1): 503–528.
- Madigan, D.; and Raftery, A. E. 1994. Model selection and accounting for model uncertainty in graphical models using Occam’s window. *Journal of the American Statistical Association*, 89(428): 1535–1546.
- Mangan, N. M.; Kutz, J. N.; Brunton, S. L.; and Proctor, J. L. 2017. Model selection for dynamical systems via sparse regression and information criteria. *Proceedings of the Royal Society A: Mathematical, Physical and Engineering Sciences*, 473(2204): 20170009.
- Messenger, D. A.; and Bortz, D. M. 2021. Weak SINDy for partial differential equations. *Journal of Computational Physics*, 443: 110525.
- Mitchell, T. J.; and Beauchamp, J. J. 1988. Bayesian variable selection in linear regression. *Journal of the american statistical association*, 83(404): 1023–1032.
- Pedregosa, F.; Varoquaux, G.; Gramfort, A.; Michel, V.; Thirion, B.; Grisel, O.; Blondel, M.; Prettenhofer, P.; Weiss, R.; Dubourg, V.; Vanderplas, J.; Passos, A.; Cournapeau, D.;

- Brucher, M.; Perrot, M.; and Duchesnay, E. 2011. Scikit-learn: Machine Learning in Python. *Journal of Machine Learning Research*, 12: 2825–2830.
- Piironen, J.; and Vehtari, A. 2017. Sparsity information and regularization in the horseshoe and other shrinkage priors. *Electronic Journal of Statistics*, 11(2).
- Raissi, M.; Perdikaris, P.; and Karniadakis, G. E. 2019. Physics-informed neural networks: A deep learning framework for solving forward and inverse problems involving nonlinear partial differential equations. *Journal of Computational Physics*, 378: 686–707.
- Ratzlaff, K. L.; and Johnson, J. T. 1989. Computation of two-dimensional polynomial least-squares convolution smoothing integrals. *Analytical Chemistry*, 61(11): 1303–1305.
- Reinbold, P. A. K.; Gurevich, D. R.; and Grigoriev, R. O. 2020. Using noisy or incomplete data to discover models of spatiotemporal dynamics. *Phys. Rev. E*, 101: 010203.
- Rudy, S. H.; Brunton, S. L.; Proctor, J. L.; and Kutz, J. N. 2017. Data-driven discovery of partial differential equations. *Science Advances*, 3(4): e1602614.
- Salvatier, J.; Wiecki, T. V.; and Fonnesbeck, C. 2016. Probabilistic programming in Python using PyMC3. *PeerJ Computer Science*, 2: e55.
- Schwarz, G. 1978. Estimating the dimension of a model. *The Annals of Statistics*, 461–464.
- Sun, L.; Huang, D.; Sun, H.; and Wang, J.-X. 2022. Bayesian Spline Learning for Equation Discovery of Nonlinear Dynamics with Quantified Uncertainty. *Advances in Neural Information Processing Systems*, 35: 6927–6940.
- Thanasutives, P.; Morita, T.; Numao, M.; and Fukui, K. 2023. Noise-aware physics-informed machine learning for robust PDE discovery. *Machine Learning: Science and Technology*, 4(1): 015009.
- Thanasutives, P.; Numao, M.; and Fukui, K. 2021. Adversarial multi-task learning enhanced physics-informed neural networks for solving partial differential equations. In *2021 International Joint Conference on Neural Networks (IJCNN)*, 1–9. IEEE.
- Tibshirani, R. 1996. Regression shrinkage and selection via the lasso. *Journal of the Royal Statistical Society: Series B (Methodological)*, 58(1): 267–288.
- Tipping, M. E.; and Faul, A. C. 2003. Fast marginal likelihood maximisation for sparse Bayesian models. In *International workshop on artificial intelligence and statistics*, 276–283. PMLR.
- Watanabe, S. 2010. Asymptotic Equivalence of Bayes Cross Validation and Widely Applicable Information Criterion in Singular Learning Theory. *Journal of Machine Learning Research*, 11(116): 3571–3594.
- Xu, H.; Chang, H.; and Zhang, D. 2020. DLGA-PDE: Discovery of PDEs with incomplete candidate library via combination of deep learning and genetic algorithm. *Journal of Computational Physics*, 418: 109584.
- Zhang, S.; and Lin, G. 2018. Robust data-driven discovery of governing physical laws with error bars. *Proceedings of the Royal Society A: Mathematical, Physical and Engineering Sciences*, 474(2217): 20180305.
- Zheng, P.; Askham, T.; Brunton, S. L.; Kutz, J. N.; and Aravkin, A. Y. 2018. A unified framework for sparse relaxed regularized regression: SR3. *IEEE Access*, 7: 1404–1423.

Supplemental Material

Generalized UBIC (G-UBIC)

The generalized UBIC (G-UBIC) is defined with a Γ scaling parameter as follows:

$$\begin{aligned} \text{UBIC}_\Gamma(\xi^k, \lambda_U) &= \text{BIC}(\xi_\mu^k) + \lambda_U \Gamma U^k \\ &= -2 \log L(\xi_\mu^k) + \log(N_\Omega) s_k + \lambda_U \Gamma U^k, \end{aligned} \quad (12)$$

where $\Gamma = \log(N_\Omega)$ results in Eq. (6). $\lambda_U \Gamma$ determines the uncertainty U^k influence on the model selection process. If the influence was given, we would easily find $\lambda_U \Gamma = \lambda_U^0 \log(N_\Omega)$, supposing that λ_U^0 were the values presented in the main text. Actually, it is not necessary to keep the influence unvaried, since we only need the appropriate model selection results, which are automatically taken care of by the Algorithm 1 that iteratively checks the likely optimal support sizes (obtained by the G-UBIC) based on the BIC improvement if we transit to the corresponding PDE model. The bound on the maximum λ_U , which preserves the impact of the log-likelihood on deciding the best PDE, is calibrated according to Γ .

$$\lambda_U^{\max} = \max_k \frac{2 \log \hat{L}(\xi_\mu^k) - \log(N_\Omega) s_k}{\Gamma U^k} \quad (13)$$

The bound is reduced to Eq. (9) with $\Gamma = \log(N_\Omega)$. As seen in Figure 5, we test the adaptability of Algorithm 1 in tuning $\lambda_U = 10^\lambda$ for the basic G-UBIC with $\Gamma = 1$. The correct identification of the true governing form is shown for every canonical PDE dataset we experimented with.

Uncertainty-penalized WAIC (UWAIC)

Demonstrating the versatility of the core proposals, we conduct a pilot extension of the uncertainty penalization to the WAIC (widely applicable information criterion) (Watanabe 2010), giving $\text{UWAIC} = T + \frac{\text{FV}}{N_\Omega} + \lambda_U \text{CV}^k$; where the T and FV are the training loss and functional variance. UWAIC is more computationally expensive than the UBIC or G-UBIC because it involves full Bayesian inference to compute the WAIC before adding the penalizing unnormalized uncertainty CV^k . The UWAIC with a λ_U specified in Figure 6 is capable of identifying the true PDE terms, similar to the UBIC. These results signify the flexibility of incorporating the proposed uncertainty penalization into other information criteria.

Sparse Bayesian Regression by Sparsifying Priors

We study the PDE discovery approach based on sparsifying priors as inspired by (Hirsh, Barajas-Solano, and Kutz 2022). Particularly, we examine sparse Bayesian regression with the spike and slap prior (SS) (Ishwaran and Rao 2005; Madigan and Raftery 1994; Mitchell and Beauchamp 1988) and the regularized (Finnish) horseshoe prior (RH) (Piironen and Vehtari 2017) to solve Eq. (3) through Bayesian inference, where we draw samples from the posterior distribution using either Markov chain Monte Carlo (MCMC) or sequential Monte Carlo (SMC) methods implemented in the PyMC package (Salvatier, Wiecki, and Fonnesbeck 2016).

For the SS prior each coefficient is given hierarchically as

$$\begin{aligned} \xi_j^{\text{SS}} | \mathcal{B}_j &\sim \mathcal{N}(\hat{\xi}_j^k, 1) \mathcal{B}_j, \\ \mathcal{B}_j &\sim \text{Bernoulli}(\beta); \end{aligned} \quad (14)$$

where β is a probability of success that characterizes the Bernoulli distribution. As a result that $\mathcal{B}_j \in \{0, 1\}$, the spike and slap prior enables sparse coefficients. Here, k should be set as the index of the maximum support sizes, depending on available computational resources.

After completing the Bayesian inference, the quantified uncertainty factor of each coefficient is given by the following calculation over its posterior samples of $\hat{\xi}_j^{\text{SS}}$:

$$U_j^{\text{SS}} = \frac{\text{CV}_j^{\text{SS}}}{\min_j \text{CV}_j^{\text{SS}}}; \quad \text{CV}_j^{\text{SS}} = \frac{\sqrt{\mathbb{V}[\hat{\xi}_j^{\text{SS}}]}}{\mathbb{E}[\hat{\xi}_j^{\text{SS}}]}. \quad (15)$$

Under our core assumption, U_j^{SS} would be comparatively low for the j^{th} effective candidate that corresponds to one of the true terms. For a candidate to be considered effective, its posterior inclusion probability (PIP) must be greater than zero. By counting the number of times a unique subset occurs in the posterior samples, we can also estimate the posterior inclusion probability (PIP) for each (best) subset. The uncertainty factor is computed likewise for the other sparsity-inducing prior (i.e., U_j^{RH} for the RH prior).

In Figures 7 and 8, the desirable outcomes are expected by inspecting that the best subsets with the correct support sizes (2 in these cases) present the highest PIPs. The marginal posterior of the negligible candidates primarily distributes a spike around the origin, whereas wider or slapped distributions are observed for the true nonzero candidates. However, achieving the results comes with the cost of setting the appropriate probability of success of the Bernoulli distribution in Eq. (14), i.e., $\beta = 0.3125$ and 0.01 respectively for the Burgers and KdV examples. If a bigger $\beta = 0.1$ is asserted for the KdV example, the best subset with the highest PIP is comprised of 3 candidates instead, which does not convey the true sparsity as shown in Figure 9, hence the troublesome sensitivity caused by β . On the contrary, the uncertainty pattern remains insensitive to the change in β from 0.01 to 0.1 . Also, the u_{xxx} and uu_x (5th and 7th) candidates yield the least uncertainty factor values. The uncertainty factors of u_{xx} and uu_x (4th and 5th candidates) are found to be minimal for the Burgers' PDE case, illustrated in Figure 7.

By the RH prior design (Hirsh, Barajas-Solano, and Kutz 2022), the coefficients sampled from the posterior distribution are not strictly sparse, exhibiting values close to, but not precisely, zero(s). Thus, a definition of pseudo-probabilities may be introduced. In this study, we are inclined to take the uncertainty factor as our preferred alternative. Figure 10 reveals that the true nonzero candidates have the lowest uncertainty factor, akin to the cases where the spike and slap priors are utilized. We set the global shrinkage parameter of the RH prior equal to 10^{-3} for both examples.

Threshold Sparse Bayesian Regression

Another approach for achieving the sparse identification of the governing PDE with quantified uncertainty (error bars)

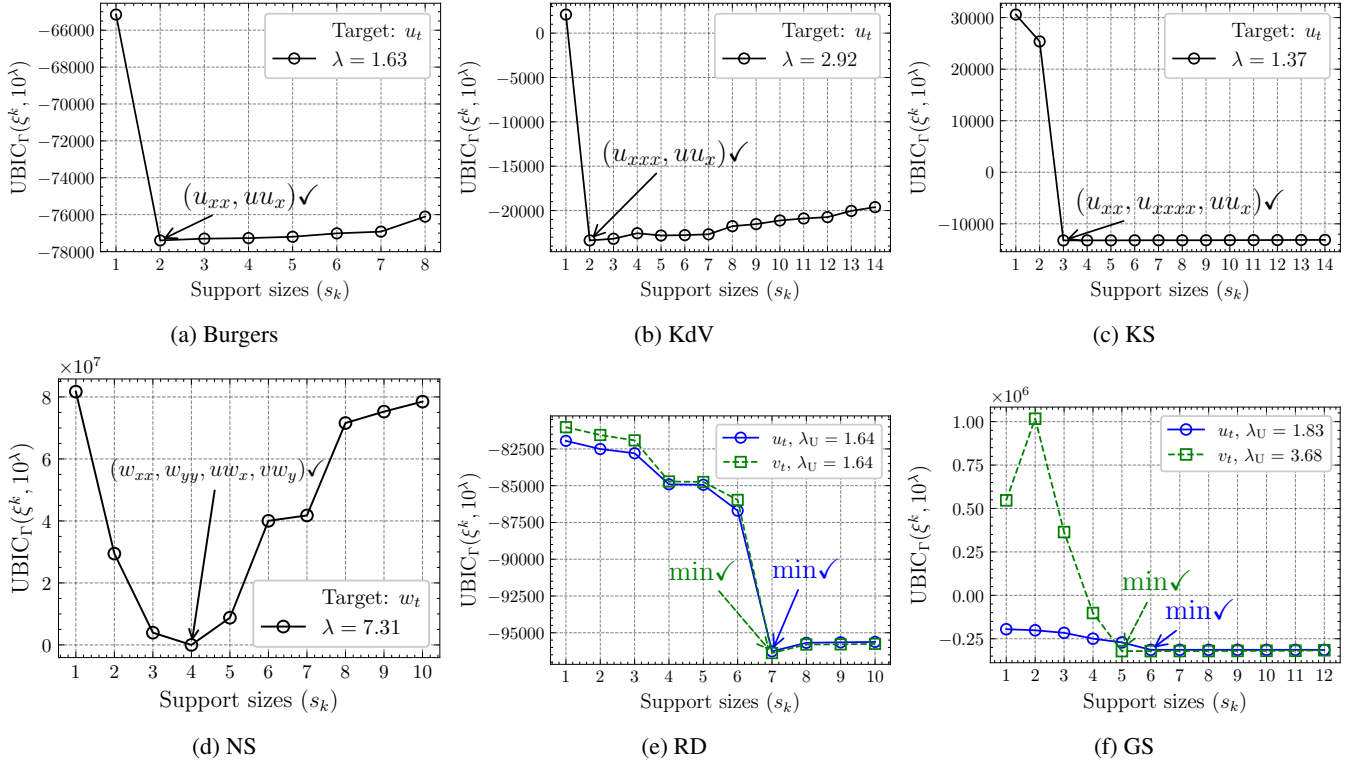


Figure 5: Successful model selection results by G-BIC with $\Gamma = 1$. In each subfigure, the (re)tuned $\lambda(s)$ is/are annotated. It should be noted all the U^k s are already given in Figure (2) and Figure (4) in the main text.

is through iterative thresholding until no further changes in sparsity are detected. This approach is known as threshold sparse Bayesian regression (Zhang and Lin 2018). We adhere closely to their iterative thresholding algorithm. In our implementation, we leveraged fast automatic relevance determination that uses sparse Bayesian learning (Tipping and Faul 2003; Faul and Tipping 2001) to estimate mean regression coefficients from the posterior distribution.

We showcase the experimental results with 3 different pre-specified threshold values, as depicted in Figure 11. We find the sensitivity with respect to the threshold: overly high or low threshold values yield underfitted and overfitted PDE models, respectively. This issue is simply addressed by aggregating the best subsets from the three cases (Threshold = $10^{-1}, 10^{-2}, 10^{-3}$) and selecting the one that minimizes the UBIC, as seen on the rightmost subfigure.

Improving PDE Discovery Accuracy

After the model selection is finalized, the coefficient values may be refitted using different candidate representations such as the convolutional weak formulation (CWF). Alternatively, we suggest that the quality of the estimated coefficients can be simply improved by further denoising on \hat{u} over a subdomain Ω_i in Eq. (3). Particularly, we specialize $\mathcal{G}_{u^+} = \mathcal{S}_{\Omega_i}^\alpha \circ \mathcal{G}_{\hat{u}}$ instead of using $\mathcal{G}_{\hat{u}}$; where $\mathcal{S}_{\Omega_i}^\alpha$ is the composite denoising function with α parameterization. Practically, $\mathcal{S}_{\Omega_i}^\alpha$ is implemented as the Savitzky-Golay filtering with the window size α and applied to the bounded \hat{u}

Table 4: Comparison based on %CE between the denoised WF and CWF methods for the library preparation. The lower %error is on **bold**.

Dataset	Denoised WF	CWF on \hat{u}	CWF on \tilde{u} (undenoised)
Burgers	0.0237	1.7287	1.2987
KdV	0.36011	1.9493	0.3215
KS	0.2738	0.3544	0.9935

over each Ω_i , before computing $\forall j, q_j^i$. Note that the order of the polynomial used for the filtering is 2. The resulting modification is called the denoised WF (weak formulation).

The comparison of how close the estimated coefficients are to the true values in terms of the average percentage coefficient error (%CE) is listed in Table 4 for the different library representations. With the simple adjustment, the denoised WF effectively outperforms the counterpart CWF method on average over the 3 PDE datasets. Basically, $\mathcal{S}_{\Omega_i}^\alpha$ could have been implemented using different denoising filters that may enhance the discovery accuracy even more. Therefore, our work demonstrates not only the effectiveness of the PDE discovery approach using the proposed UBIC but the accurately estimated coefficients.

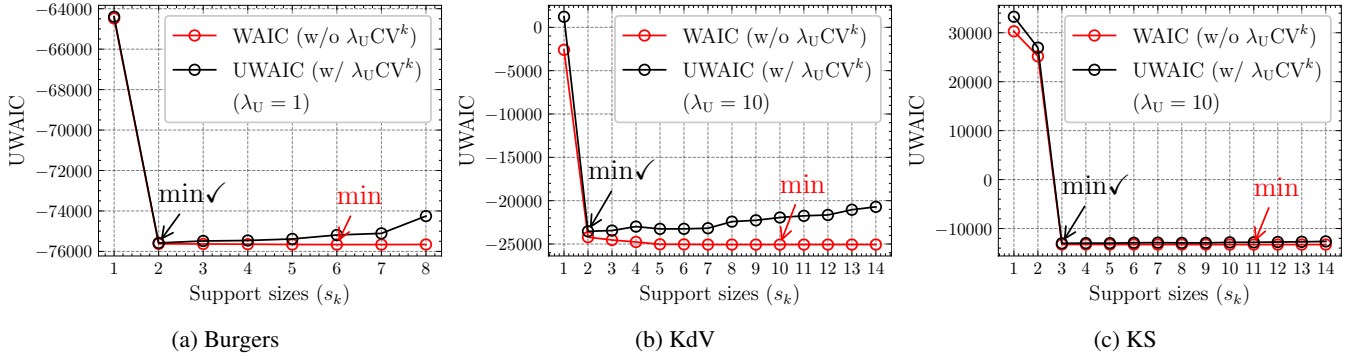


Figure 6: Extension to the uncertainty-penalized WAIC (UWAIC)

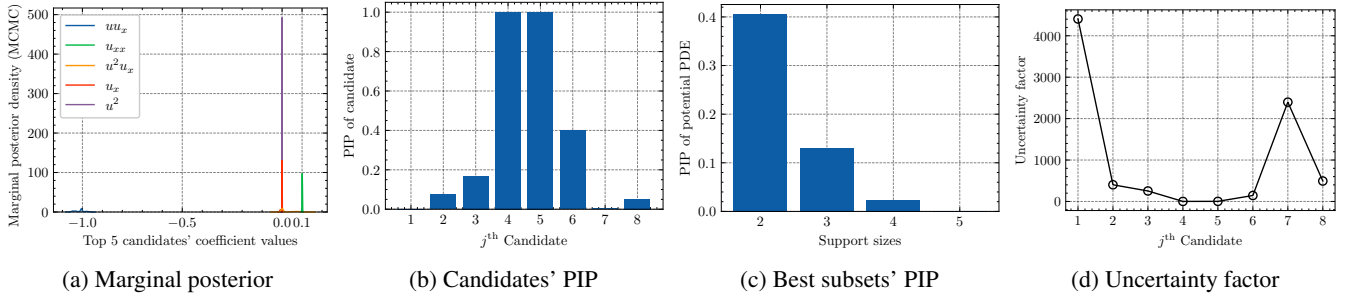


Figure 7: Sparse Bayesian regression with the SS prior ($\beta = 0.3125$) for discovering the Burgers' PDE. The candidates are listed in the following order: $[u, u^2, u_x, u_{xx}, uu_x, u^2u_x, uu_{xx}, u^2u_{xx}]$.

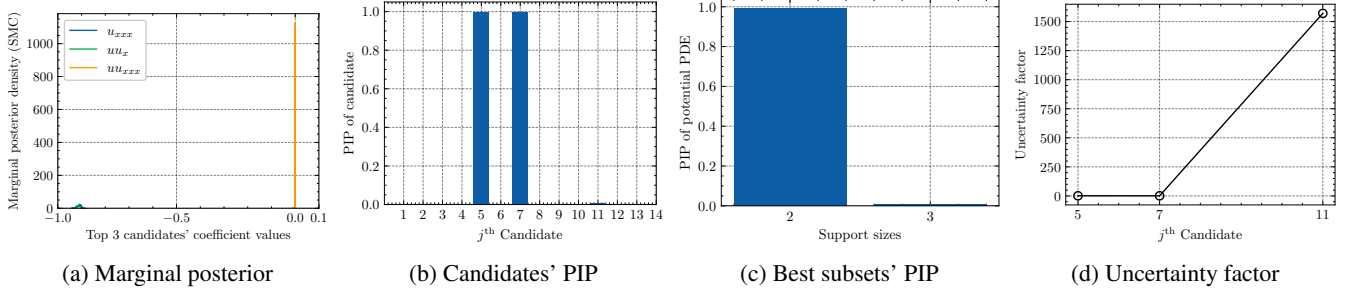


Figure 8: Sparse Bayesian regression with the SS prior ($\beta = 0.01$) for discovering the KdV PDE. The candidates are listed in the following order: $[u, u^2, u_x, u_{xx}, u_{xxx}, u_{xxxx}, uu_x, u^2u_x, uu_{xx}, u^2u_{xx}, uu_{xxx}, u^2u_{xxx}, uu_{xxxx}, u^2u_{xxxx}]$.

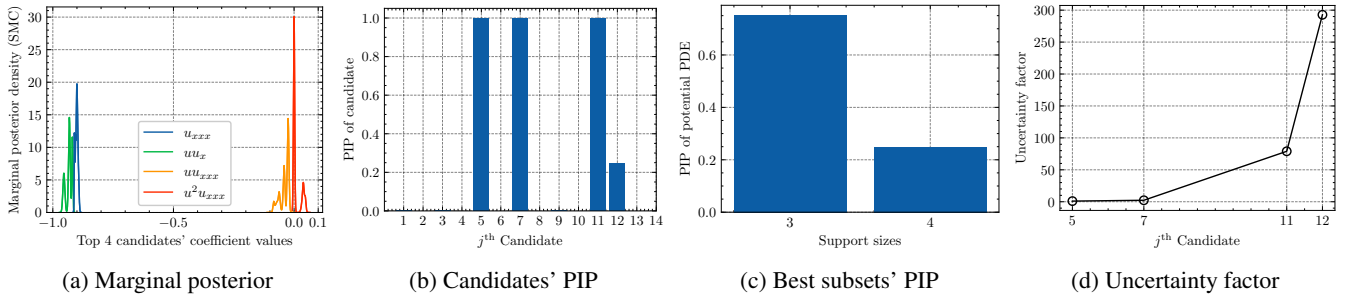


Figure 9: Sparse Bayesian regression with the SS prior ($\beta = 0.1$) for discovering the KdV PDE. Please refer to the candidate order listed in Figure 8.

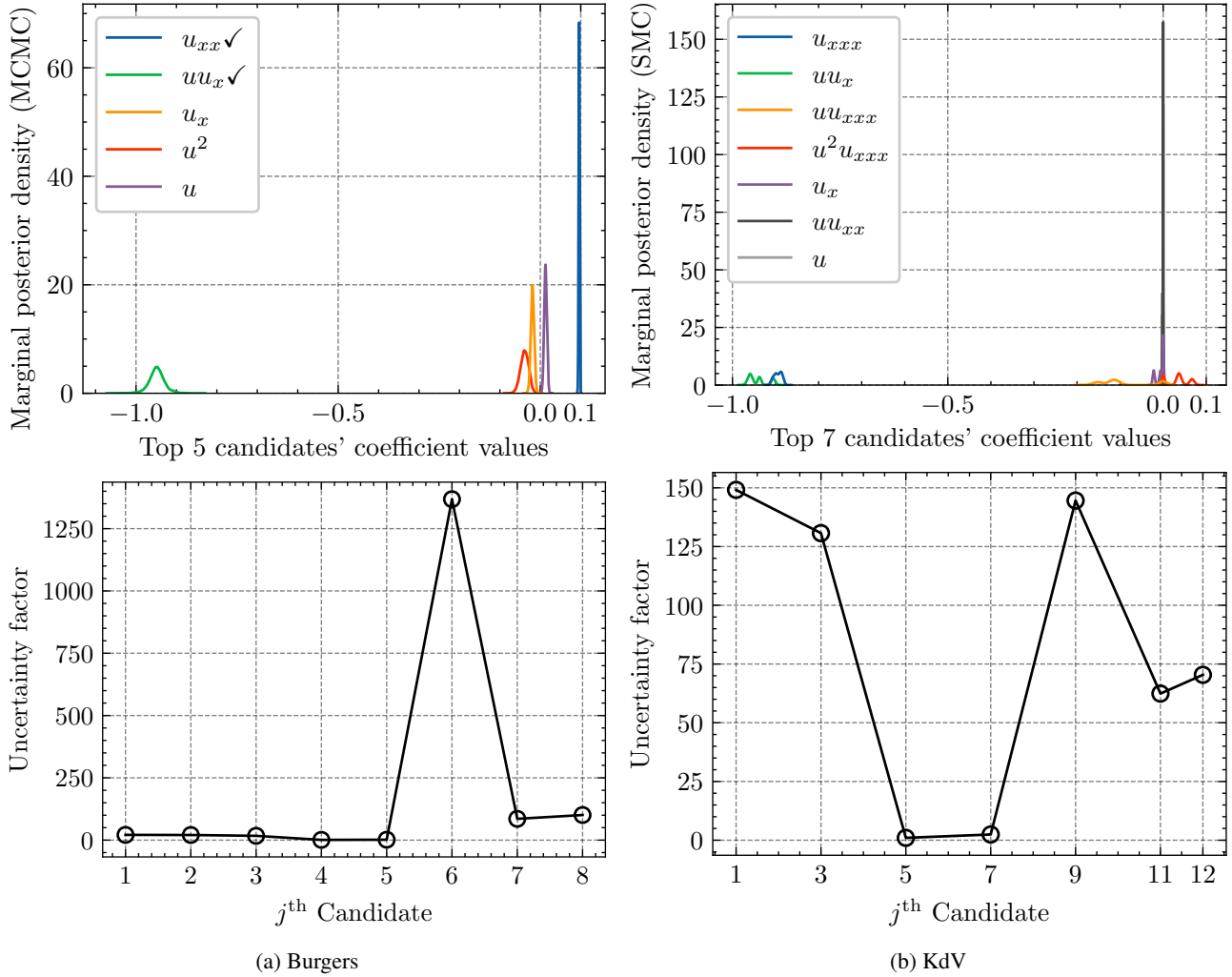


Figure 10: Sparse Bayesian regression with the RH prior for discovering the Burgers and KdV PDE. The global shrinkage parameter is set equal to 10^{-3} . Please refer to the candidate order listed in Figures 7 and 8.

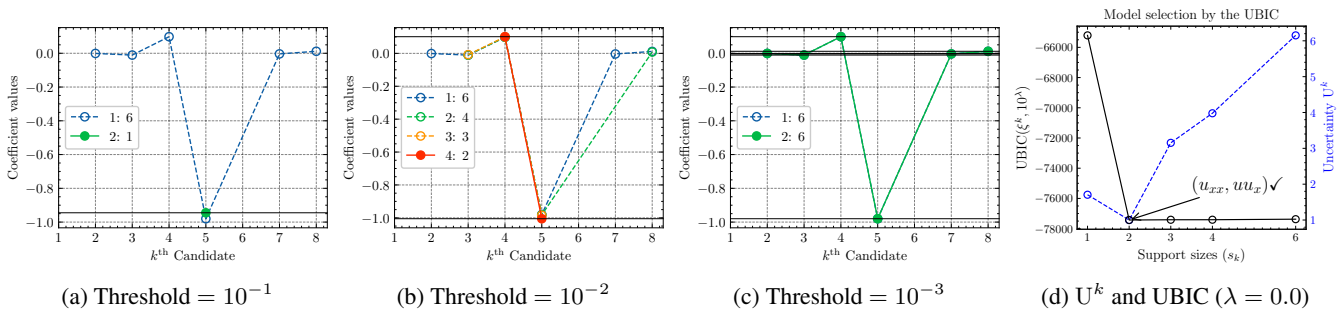


Figure 11: Threshold sparse Bayesian regression for discovering Burgers' PDE. Please refer to the candidate order listed in Figures 7.

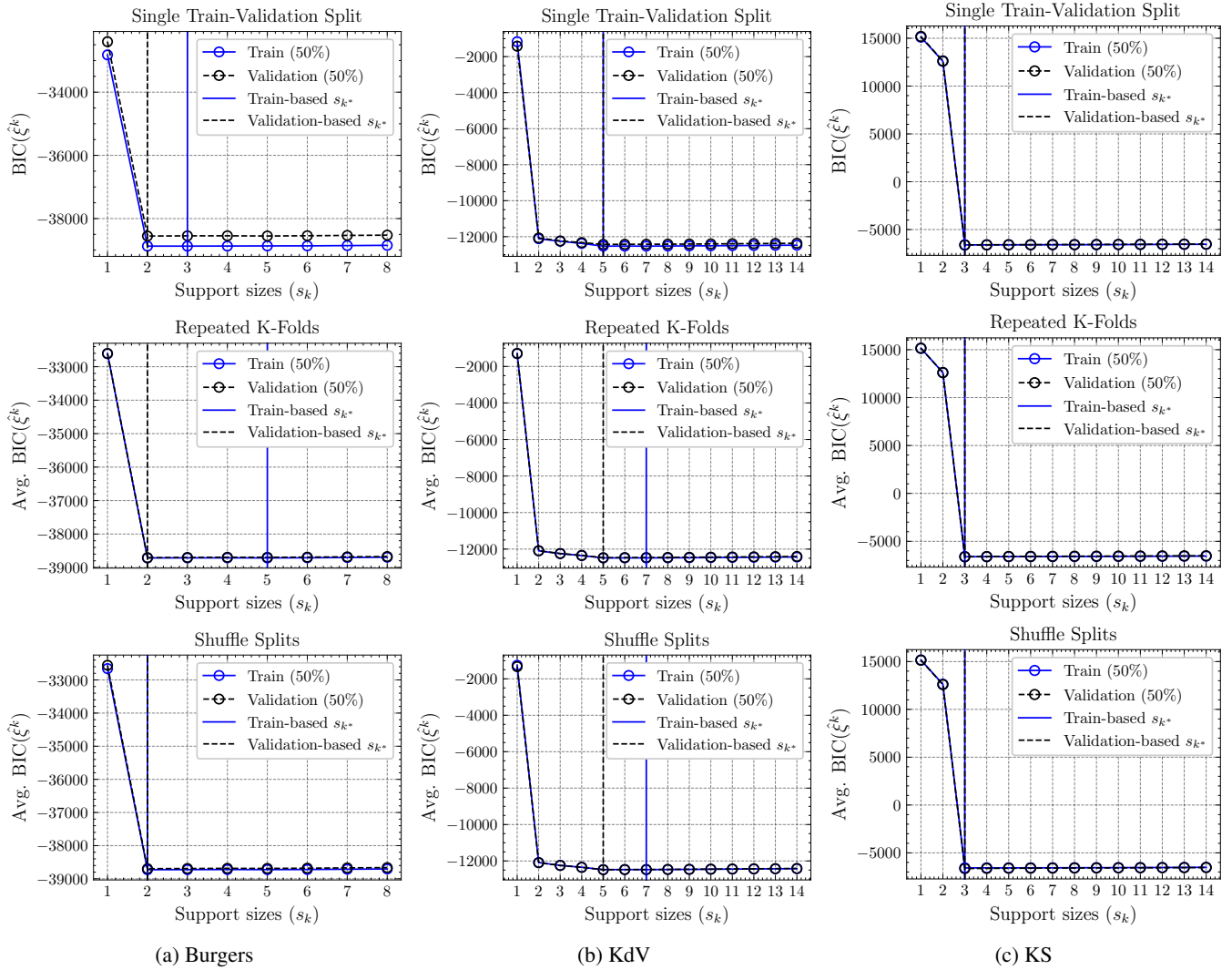


Figure 12: Cross-validation model selection (finding the optimal support sizes) for Burgers, KdV, and KS examples.

Cross-Validation Pitfalls

One might intuitively presume that the cross-validation strategy would suffice for selecting the optimal support sizes from Eq. (4). To validate this assumption, we conducted experiments using various data splitters available in the Scikit-learn package (Pedregosa et al. 2011). Specifically, we tested the following splitter classes, which are represented respectively in the middle and bottom rows of Figure 12.

- `RepeatedKFold(n_splits=2, n_repeats=5)`
- `ShuffleSplit(n_splits=2, n_repeats=10)`

The former splitter was configured with 2-folds and repeated 5 times with different randomization in each repetition. Contrarily, the latter splitter was configured with 10 re-shuffling and splitting iterations but did not guarantee that all folds are different. We employed the single train-validation split procedure, as depicted in the first row of Figure 12, wherein the first half of the samples were allocated for training and the second half for validation.

In the Burgers and KS cases, the utilization of validation sets safeguards against the wrong selection of the overfitted PDEs. Nevertheless, none of the splitters were found effective for the KdV example, where there are the noticeable BIC drops observed during the transition from the 2-support PDE to the 5-support PDE. We label this scenario as the “cross-validation pitfalls”, which could have led us to the misconception that the 5 support sizes are optimal.

Robust Adaptive Model Selection

We evaluate the feasibility of our proposed methods in highly noisy scenarios. We ran through the Burgers, KdV, and KS examples with higher levels of noise but, this time, we ablated the denoising step to first justify solely the usability of the UBIC. Surprisingly, we realized that using just the weak formulation and selecting based on the adaptive UBIC, we can truly identify the governing PDEs even under the very high noise levels, as illustrated in Figure 13. The

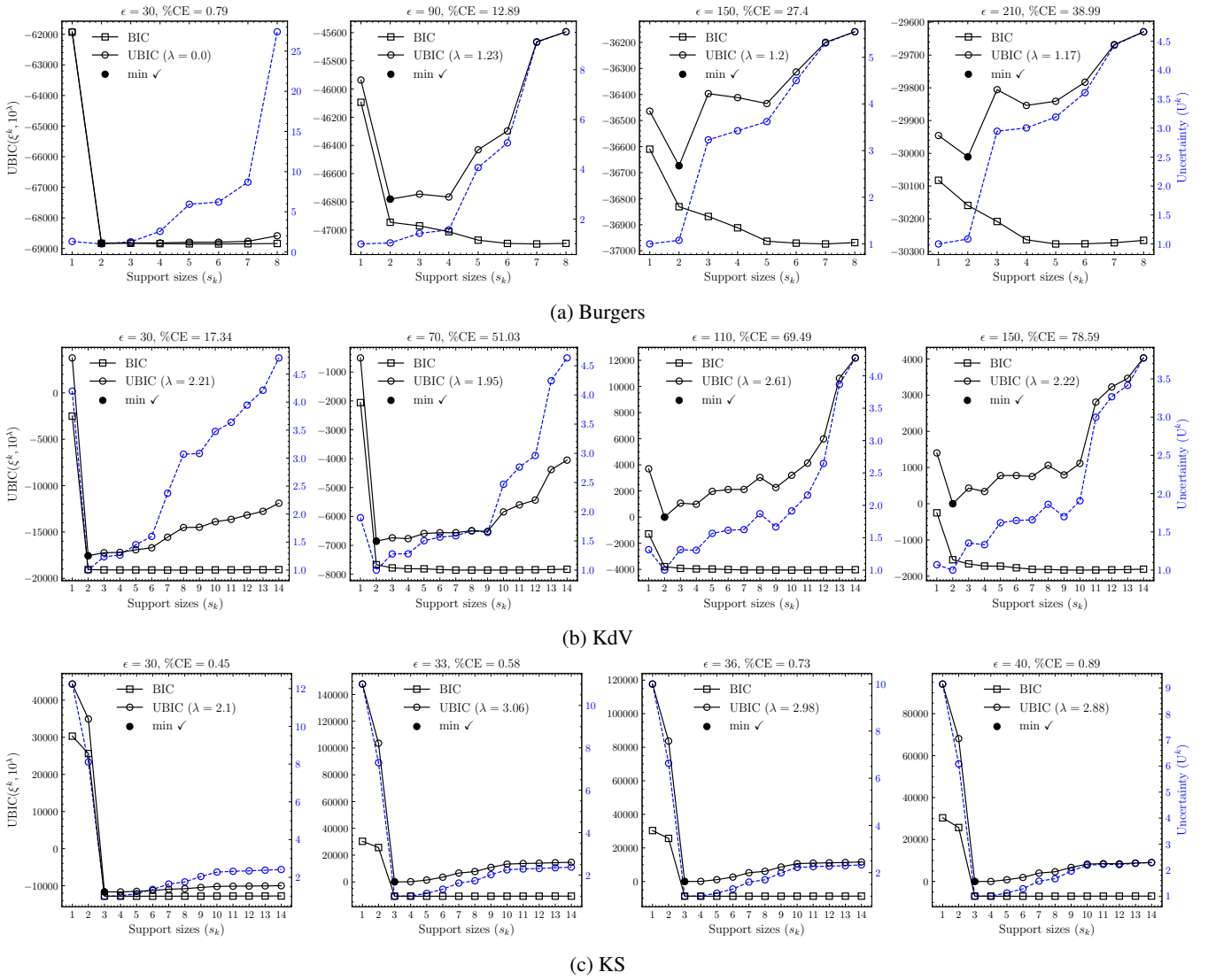


Figure 13: Robust model selection by the UBIC without preceding denoising under the highly noisy scenarios. For the Burgers and KS cases, we assign $\tau_0 = P_{75}(S)$. For the KdV cases in this Figure, we assign $\tau_0 = P_{85}(S)$.

outcomes emphasize the advantage of incorporating penalizing uncertainty information for the model selection, especially in the scenarios contaminated with substantial noise.

Simulation-based Model Selection: Extended Results

The evidence presented in Table 3 indicates that the s_k -support PDE has sufficient complexity to generate the lower-BIC simulated state variable compared to the s_{k+1} -support PDE, as demonstrated via the PINN learning. To strengthen the results, we also solve the PDEs on their entire spatio-temporal domain using the Chebfun and Dedalus software, unlike the PINN approach that necessitates a train-validation data split. The PySR package (Cranmer 2023) is used to recover the analytical equation of the initial condition. The results are given in Table 5, revealing the same conclusion.

Table 5: Simulation-based model comparison between the two likely PDEs, whose support sizes are s_{k^*} and s_{k^*+1} .

Dataset	PINN ¹	Dedalus	Chebfun
Burgers $s_{k^*} = 2$	-16439	-134490	-134490
$s_{k^*+1} = 3$	-2020	-134150	-134160
KdV $s_{k^*} = 2$	247070	-731845 ²	-708492 ²
$s_{k^*+1} = 3$	280799	-722890	Divergence ³
KS $s_{k^*} = 3$	339036	783459	819638
$s_{k^*+1} = 4$	501440	811910	819650

¹The simulated solution by PINN is evaluated on the validation set D_{val} detailed in Table 6, unlike the full-domain simulated solutions by Dedalus or Chebfun, which get evaluated on the entire domain.

²The 2-support PDE is added with an intercept and refitted using CWS before the simulation. ³The solution by the spin function explodes (diverges) with a small time-step of 10^{-5} .

Table 6: Nonoverlapping train and validation domains particularly bounded for performing the PINN-based model selection.

Dataset	$\mathcal{D}_{\text{Train}}$		\mathcal{D}_{Val}	
	x	t	x	t
Burgers	$[-8, 0]$	$[0, 5]$	$[0.0625, 7.9375]$	$[5.1, 10]$
KdV	$[-20, 19.84]^1$	$[20.08, 40]$	$[-19.92, 19.92]^2$	$[0, 20]$
KS	$[0.0982, 50.36]$	$[0, 50]$	$[50.46, 100.53]$	$[50.4, 100]$

¹From even indices of the discretized x . ²From odd indices of the discretized x .

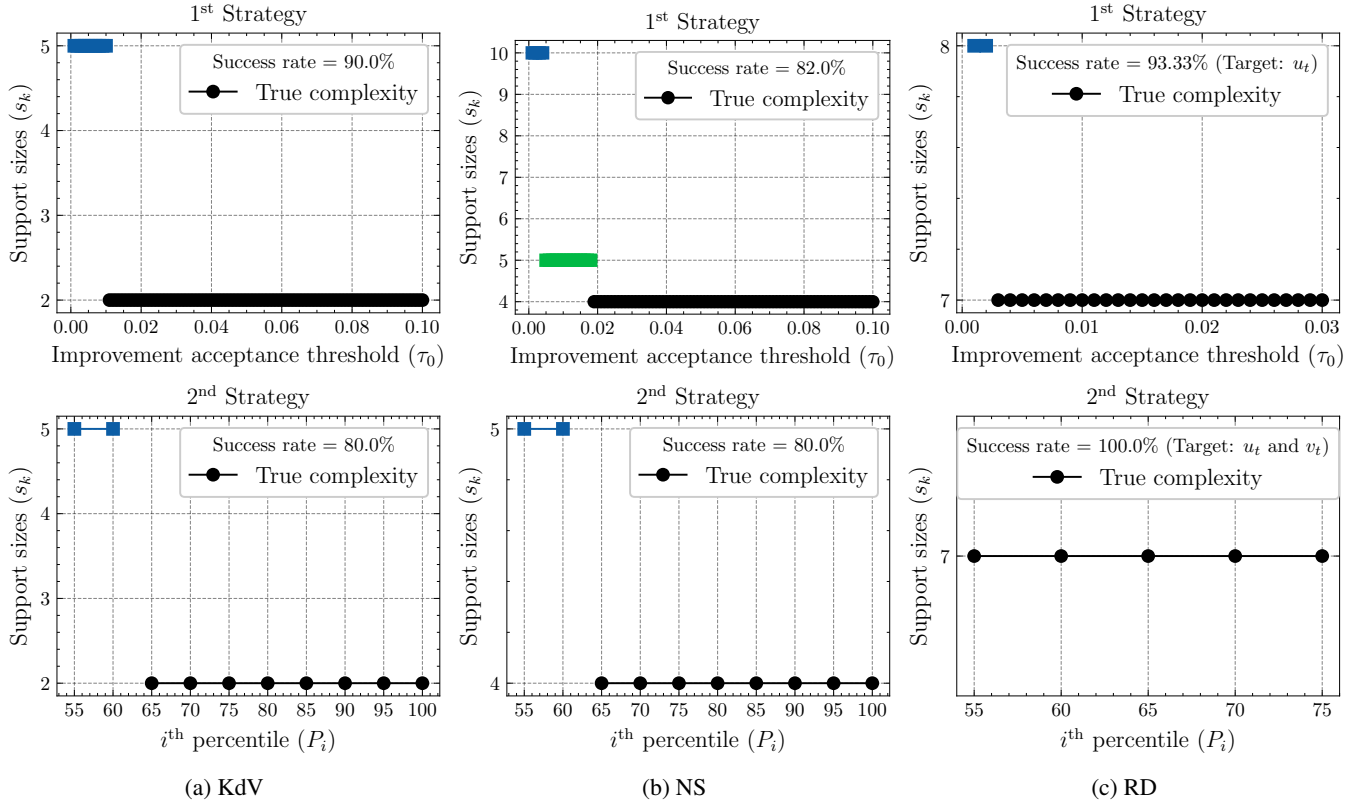


Figure 14: Sensitivity analysis on the KdV, NS, and RD examples, where one (or both) of the success rates of the strategies falls below 100%.

Sensitivity Analysis

In this analysis, we assess the sensitivity of the proposed Algorithm 1 by its success rate in identifying the true equation under different values of τ_0 . Recall that we mention the two distinct strategies for assigning τ_0 values that result in the selection of PDEs whose support sizes are greater than one: (i) using raw numerical values and (ii) adopting percentiles of successive improvement factors S (refer to the main text), considering only BIC-decreasing models. The strategies, on which we mainly focus, are given in what follows.

- (i): $\tau_0 = 10^{-3}(1 + h)$; where $h \in \{0, 1, 2, \dots, 99\}$.
- (ii): $\tau_0 = P_i(S)$; where $i \in \{55, 60, 65, \dots, 100\}$.
 P_i calculates the i^{th} percentile of the set S .

The success rate of each strategy is quantified as the number of times we successfully identify the true equation form over the number of all τ_0 values that lead to the selection of PDEs

whose support sizes (s_k) is more than one (to avoid overly high values of τ_0).

We achieve the perfect 100% success rate for some of the examples listed in Table 1. For the examples, in which the success rates are less than 100% using one of the strategies, we create Figure, showing the suggested support sizes (by Algorithm 1) against the τ_0 values within the specified range. In spite of the possible inappropriate uses of excessively low τ_0 that causes the selection of overfitted PDEs, the success rates exceeding 80% are deemed acceptable, implying the manageably low sensitivity of the Algorithm 1.

Data and Code Availability

Please find the accompanying data and code made available at <https://github.com/Pongpisit-Thanasutives/UBIC>. We provide 2D visualization of the dataset files we experimented with in Figure 15.

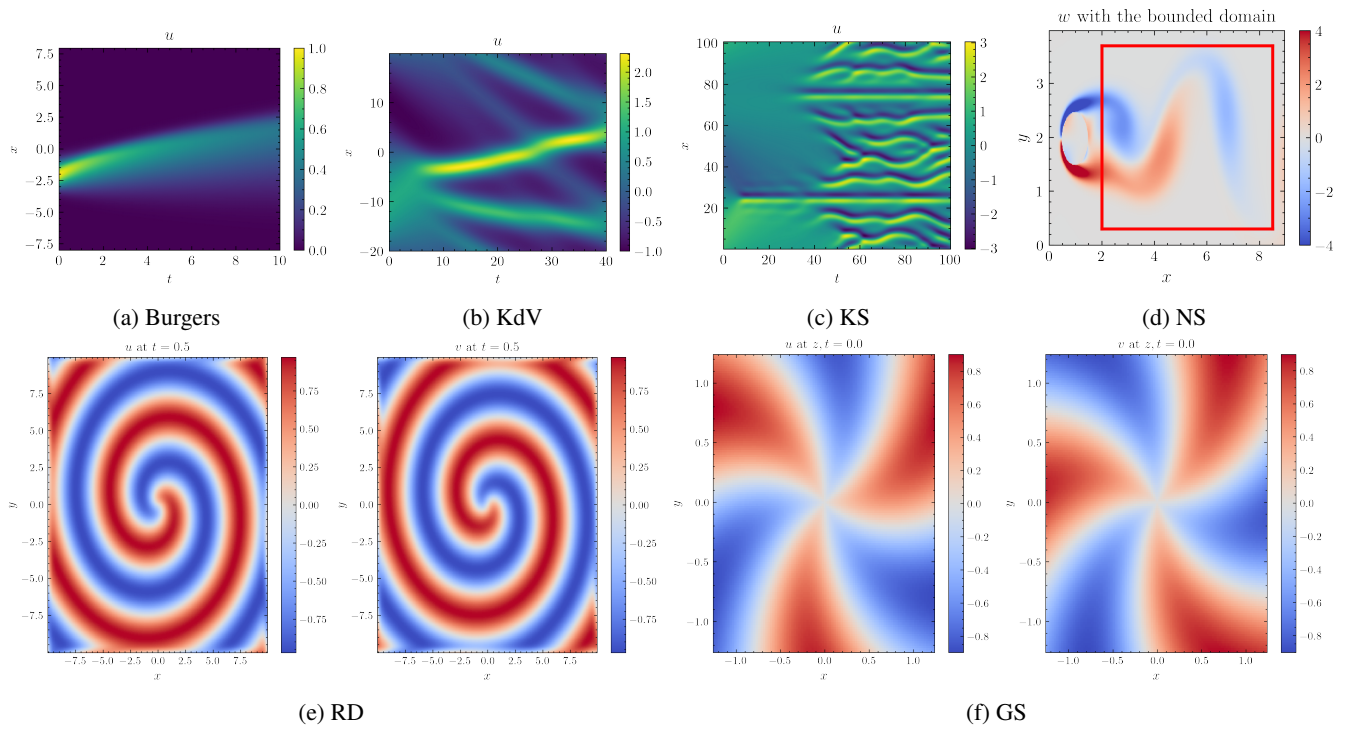


Figure 15: Dataset visualization